RESEARCH ARTICLE

Key Points:
- Optical, ionosonde, and meteor radar observations of non-underdense (transitional and overdense) meteor trails were made at high latitude
- During the first 4 min the decay rate of ionosonde echo depends on initial electron line density of trails (empirical dependence obtained)
- Meteor events were accompanied by nonspecular long-lived detections using a colocated meteor radar with operating frequency 36.9 MHz

Correspondence to:
A. Kozlovsky,
alexander.kozlovsky@oulu.fi

Multi-Instrumental Observations of Nonunderdense Meteor Trails

A. Kozlovsky[1] [iD]**, S. Shalimov[2,3,4], J. Kero[5]** [iD]**, T. Raita[1]** [iD]**, and M. Lester[6]** [iD]

[1]Sodankylä Geophysical Observatory, Sodankylä, Finland, [2]Institute of Physics of the Earth RAS, Moscow, Russia, [3]Space Research Institute, Moscow, Russia, [4]National Research Center "Kurchatov Institute", Moscow, Russia, [5]Swedish Institute of Space Physics, Kiruna, Sweden, [6]Department of Physics and Astronomy, University of Leicester, Leicester, UK

Abstract Using data from the Sodankylä Geophysical Observatory (67°22′N, 26°38′E, Finland) meteor camera from the whole year 2015, we identified and investigated 28 optical meteors with accompanying ionization trails unambiguously detected by the Sodankylä Geophysical Observatory ionosonde, which sounded the ionosphere once per minute with frequency rising from 0.5 to 16 MHz. These ionosonde reflections were obtained from heights around 90 km. The electron line densities of the trails were found to be between 10^{14} and 10^{16} m^{-1}, which characterize the trails as nonunderdense (i.e., transitional and overdense). The ionosonde reflections were observed for a few minutes, with decreasing maximal frequency of the return. During the first 250 s, for the trails with initial line density about $(2-3) \cdot 10^{15}$ m^{-1} the return frequency decreased with time corresponding to the diffusional expansion of cylindrical meteor trails, that is, $f \propto t^{-\gamma}$, where the exponent $\gamma = 0.5$, whereas less dense trails decayed slower ($\gamma \approx 0.2$) and more dense trails decayed faster ($\gamma \approx 1$). In many cases the meteor events were accompanied by nonspecular long-lived detections using a colocated all-sky interferometric meteor radar with operating frequency 36.9 MHz. As a rule the meteor radar echo durations were longer than expected from diffusional expansion of cylindrical meteor trails and their amplitudes were highly variable. We suggest that the slower frequency decrease of the ionosonde echoes and the nonspecular long-lived meteor radar echoes might be associated with the presence of meteoric dust.

1. Introduction

Echo traces that look like echoes from sporadic E layers (Es) are often observed in the data from ionosondes sounding (ionograms) obtained during meteor showers. According to Ellyett and Goldsbrough (1976) and Maruyama et al. (2003), such echo traces may be classified into three types. First, when a single meteoroid enters the atmosphere, it produces ionization, which may backscatter the ionosonde radio waves. Second, enhancement of the E layer electron density and corresponding ionosonde echoes may be due to an immediate effect of the total ionization created by many meteors. Third, meteors bring metallic ions to the ionosphere and sporadic E layers may be formed due to subsequent action of wind shear on the meteor ion concentrations. In the present paper we focus on the first type of traces in the ionosonde data.

Basics of the physics of meteor trails may be found in Bronshten (1983). A meteoroid entering the atmosphere produces a cylindrical ionized trail, typically at heights between 80 and 100 km, which correspond to the mesosphere or lower thermosphere region. A radio wave with a wave vector, which is perpendicular to the trail, may be backscattered, which is called specular reflection. As the trail is expanding due to diffusion, the ionosonde starts to receive an echo at a certain frequency at the time when the diameter of the trail reaches the corresponding wavelength. At this time, the power of the echo sharply increases up to its maximum value. If the electron density in the trail at this time is such that the plasma frequency is larger than the wave frequency, the trail is called overdense. The electron line density, α_l, of an overdense trail exceeds a certain value, α_c

$$\alpha_l > \alpha_c = 2.4 \cdot 10^{14} \text{m}^{-1} \tag{1}$$

The echo power stays at or near the maximum level for a time during which the plasma frequency in the expanding trail decreases to the wave frequency, after which the echo decays. The duration of the radio echo from an overdense trail at frequency f is given by

$$\tau = \frac{r_e c^2}{4\pi^2 f^2} \frac{\alpha_l}{D} \tag{2}$$

where $r_e \cong 2.82 \cdot 10^{-15}$m is the classical electron radius, c is the speed of light, and D is a diffusion coefficient.

If the electron line density in a trail is less than α_c, such a trail is called underdense. Just after the sharp increase to a maximal value, the amplitude of the radio signal backscattered from an underdense trail decays exponentially:

$$A(t) = A(0) \exp\left(\frac{16\pi^2 f^2 D}{c^2} t\right) \tag{3}$$

While the backscattering from overdense trails is a reflection from a surface (like the Fresnel reflection from a mirror), the backscattering from underdense trails is incoherent scatter on electrons of the radio wave penetrating into the ionized trails. Trails with an electron line density that is close to α_c are intermediate or transitional.

Diffusion is the predominant mechanism in the decay of meteor trails. However, other factors like turbulence of neutral atmosphere (Kelley et al., 2003), wind shear (Maruyama et al., 2003), presence of dust particles (Chau et al., 2014; Shalimov & Kozlovsky, 2015), and recombination (Kim et al., 2012; Lee et al., 2013) may contribute to the decay time as well. Hence, meteor-induced traces in ionosonde data can provide important information for studying the mesosphere and lower thermosphere region.

Ionosondes transmit radio waves in a frequency range between 0.5 and 30 MHz, so that the duration of echoes from meteor trails may be from a few to 10–20 min. This requires rapid-run ionosonde observations, that is, a sounding rate of once per minute, whereas routine ionosonde sounding is typically made once 15 or 30 min. In the last decades only some short campaigns for rapid-run ionosonde observations of meteors were performed during the Leonid (Maruyama et al., 2003) and Perseid (Maruyama et al., 2008) meteor showers.

At the Sodankylä Geophysical Observatory (SGO, 67°22′N, 26°38′E, Finland) ionosonde sounding has been routinely made once a minute since April 2007. Additionally, an all-sky interferometric meteor radar (SKiYMET) has been routinely operating at SGO since December 2008 and an optical meteor camera running in a suitable mode in 2015. In the present paper we report the results of these multi-instrumental observations of meteor trails.

2. Meteor-Induced Traces in the Ionosonde Data

Sodankylä Geophysical Observatory is located in the auroral zone with a corrected geomagnetic latitude of 64°. Ionosonde observations have been performed at SGO since the International Geophysical Year 1957. The present ionosonde, called Alpha Wolf, is a frequency-modulated continuous wave chirp sounder developed at SGO. Details of the instrument have been described in Enell et al. (2016). Sounding is made once a minute, and each sweep lasts for 30 s, during which the transmitted signal frequency is linearly increased from 0.5 to 16 MHz.

As an example, Figure 1 presents a sequence of o-mode ionograms from 12 December 2015 showing the appearance of a meteor-induced trace. In the ionogram taken at 1437 UT (Figure 1a) there were no indications of E layer reflections at frequencies higher than 1 MHz. In the next minute, at 1438 UT (Figure 1b), the meteor-induced trace (Em) was clearly detected at the virtual height near100 km where waves at frequencies up to about 4.5 MHz were reflected (i.e., foEm = 4.5 MHz at that time). One minute later (1439 UT, Figure 1c), the maximal reflected frequency was about 2.5 MHz, at 1440 UT it decreased to about 2 MHz (not shown here), and finally, at 1441 UT (Figure 1d) the meteor-induced trace had disappeared. Thus, the lifetime of the trace was less than 3 min.

Signatures of meteor-induced traces are clearly visible in the frequency-time-intensity (FTI) plots, which are made at SGO for monitoring the critical frequency of the ionospheric E layer (foE) and also sporadic E layers (foEs; Kozlovsky et al., 2014). From each ionogram, we take for each frequency the pixel of maximal power reflected from the height range 80–130 km. Then, these rows obtained from individual ionograms are turned vertical and placed side by side to obtain time profiles with color-coded signal intensity and frequency on the
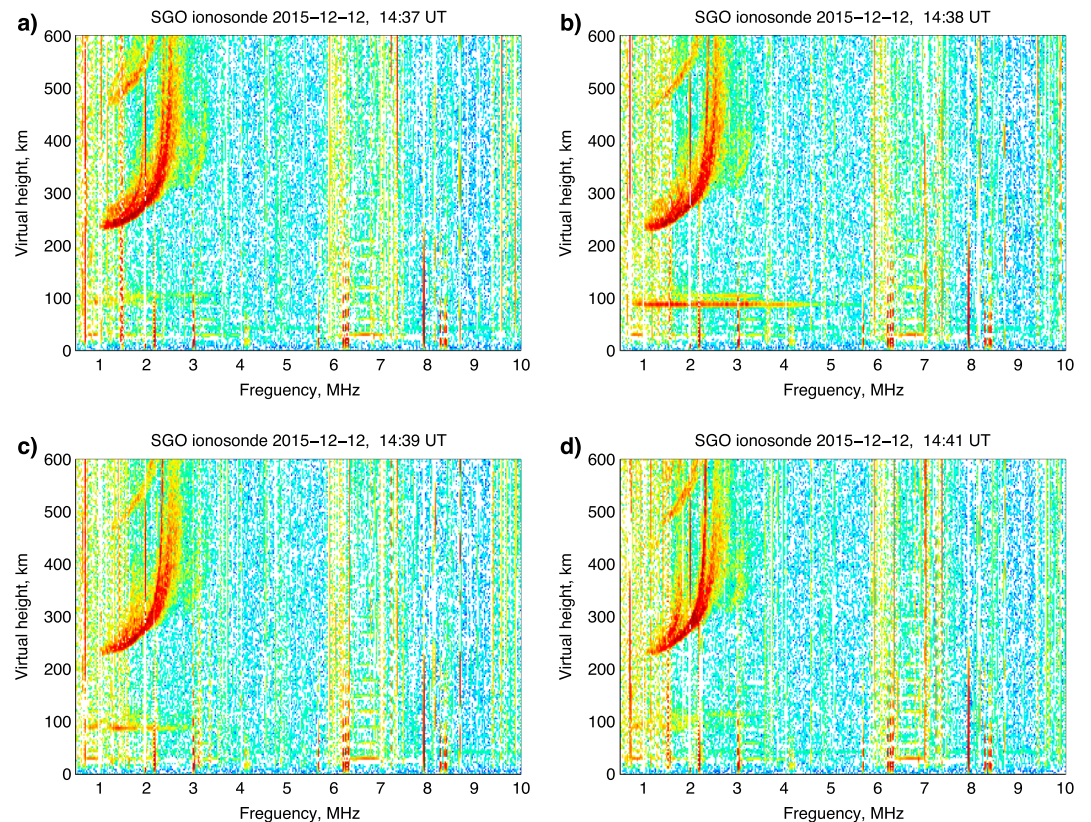
Figure 1. A sequence of *o*-mode ionograms from 12 December 2015 showing appearance of the meteor-induced trace: (a) 1437 UT—no indications of *E* layer reflections at frequencies higher than 1 MHz; (b) 1438 UT—the meteor-induced trace at the virtual height near 100 km, frequencies up 4.5 MHz are reflected; (c) 1439 UT—the maximal reflected frequency about 2.5 MHz; and (d) 1441 UT—the meteor-induced trace has disappeared.

vertical axis. An example is shown in Figure 2a. This FTI plot provides an overview of sporadic *E* layers for the whole day of 12 December 2015, which was during the Geminid meteor shower. There are numerous short-lived, one to few minutes, sporadic *E* layers (like, e.g., at 1438 UT corresponding to the ionograms in Figure 1), which are caused by meteors. Sometimes, like, for example, at 1821 UT, waves at frequencies as high as 16 MHz were backscattered from meteor trails.

Other features seen in the daily FTI plot in Figure 2a are signatures of the nightside auroral precipitation between 00 and 02 UT, around 20 UT, and around 2130 UT. In the daytime between 0730 and 1230 UT there were no echoes from the *E* region because of radio wave absorption. Both the enhanced auroral activity and the absorption were likely due to the high-speed stream of solar wind at that time.

Similar to the FTI plots, we also make height-time-intensity (HTI) plots for monitoring the virtual height of reflections. The HTI plots are color-coded plots of the intensity of the reflected signal at a fixed frequency in a frame of time and virtual height. Such plots are created by extracting vertical pixel columns at a fixed frequency from individual ionograms and putting the columns side by side (Kozlovsky et al., 2013, 2014). An example of HTI plot for the whole day of 12 December 2015 is shown in Figure 2b. The horizontal axis is the time, and the vertical axis is the virtual height. Traces of reflection from meteor trails are seen in the HTI plot near 90 km or above. The HTI plot shows the virtual height of reflectors, which may be equal to the true height only if the reflector is in zenith. The true height of the meteor trails is discussed further in section 4.

3. Optical Observations of Meteors

Optical observations of meteors are made with the SGO meteor camera (MC) installed in a dome at the SGO field station Pittiövaara a distance of about 10 km from the ionosonde. The main target of the system is to
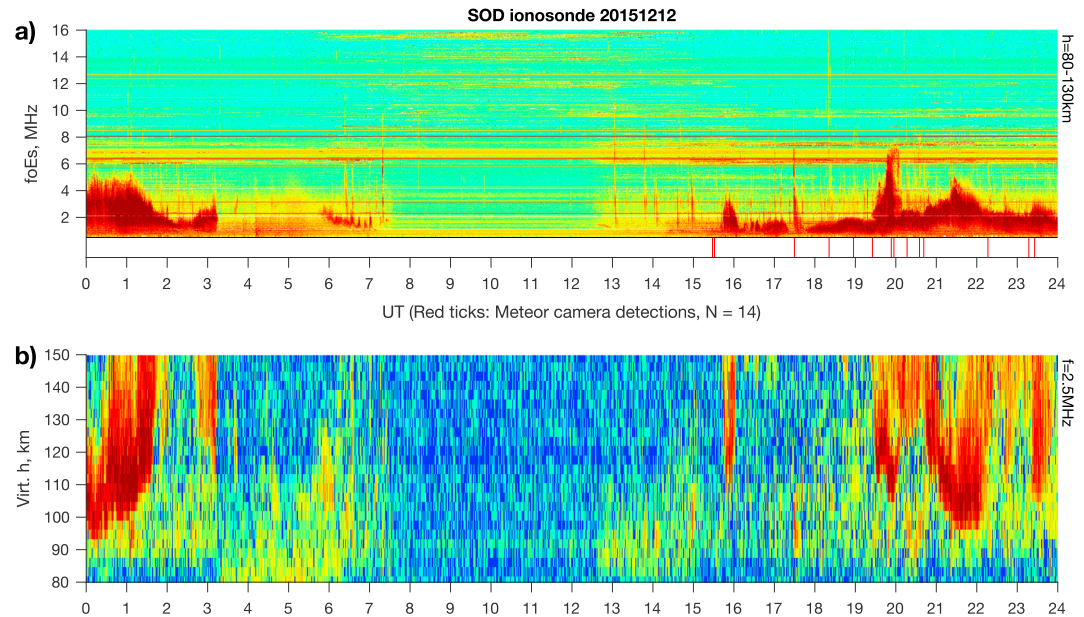
Figure 2. Overview plot of SGO ionosonde data for the whole day of 12 December 2015: (a) a color-coded plot of the maximal intensity of the reflected signal in a fixed range of virtual height (80–130 km) in the time and frequency frame (FTI plot). Red ticks above time axis indicate times of the meteor camera detections; (b) a color-coded plot of the intensity of the reflected ionosonde signal at a fixed frequency (2.5 MHz) in the time and virtual height frame (HTI plot).

capture and record bright meteors, fireballs, the brightest of which are able to produce meteorite falls. Before 2015 the camera was pointed toward the south to facilitate common volume observations with the Finnish Fireball Network. The network has recently grown to monitor a surface of more than 400,000 km^2 with most of the observations made by amateur astronomers (Gritsevich et al., 2014). In 2015 the MC was repointed toward the zenith to improve conditions for the present study. The camera is an analogue Watec 902H3 Ultimate with Fujinon CCTV lens YV2.8 × 2.8SR4A-SA2, giving field of view of about 112° × 81°. It uses an automatically controlled electronic iris and shutter speed to enable continuous nighttime and daytime observations. The iris and shutter are adjusted in accordance with the real-time light intensity, and the exposure time of each frame therefore varies in the range between 1/50 s and 1/100,000 s. The system is turned off during polar summer so that no observations are made from the end of April to early August. The camera recordings are of Phase Alternating Line format with a standard video rate of 25 Hz, which means that one frame is taken each 40 ms. The video stream is fed into an automatic meteor detection and analysis software developed for and maintained by the Swedish Meteor Allsky Network (Stempels & Kero, 2016). For every event identified as a meteor, a sequence of frames is archived and the position of the meteor at each frame (azimuth and elevation) is determined. An example of a meteor observation is shown in Figure 3, which is a sum of 24 frames taken during 0.95 s from 17:29:43.34 to 17:29:44.29 UT on 12 December 2015.

During the whole year 2015, 317 meteor events were identified in the meteor camera data. We indicated the time of these events at the ionosonde daily FTI plots. For instance, red ticks above the time axis in the FTI plot in Figure 2a indicate MC meteor detections on 12 December 2015. There were 14 meteors detected optically during this day, whereas the number of meteor traces in the ionosonde data is much larger. There are at least two obvious reasons for why only a few of the
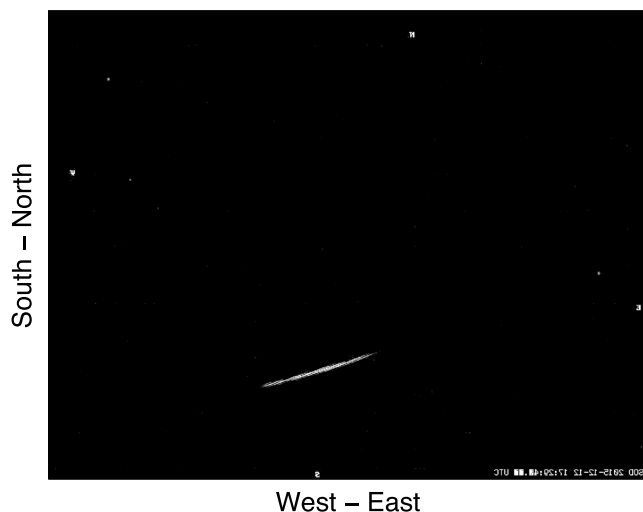

Figure 3. An example of meteor camera observation on 12 December 2015: (a) sum of 24 frames taken during 0.95 s from 17:29:43.34 to 17:29:44.29 UT.

Table 1
Data of Meteors From Optical and Ionosonde Observations

Meteor camera				Ionosonde				Ionosonde and meteor radar		
Day and time	tc (ms)	El. (deg.)	Az. (deg.)	H (km)	ti (s)	f_{max} (MHz)	f_{min} (MHz)	$D(H)$ (m^2/s)	α_{IO} (10^{15} m^{-1})	τ_{MR} (s)
25 Jan 21:33:34	480	76–81	156–176	82.3 ± 0.5	504	13.3	2.5	3.3	4.24	6.0
21 Aug 22:06:25	240	69–71	203–215	92.0 ± 0.7	333	7.8	2.1	6.4	2.68	2.0
25 Aug 00:11:37	320	72–80	348–349	92.1 ± 0.8	622	8.5	2.3	6.3	2.40	1.8
27 Oct 02:22:14	380	71–73	75–107	88.3 ± 0.2	582	4.0	1.4	4.9	0.43	0.4
27 Oct 19:24:09	60	73–74	229–230	106.0 ± 0.2	351	4.4	2.1	11.7*	1.89*	0.8
28 Oct 02:56:18	540	68–83	41–70	89.3 ± 2.0	459	5.8	1.8	5.4	0.61	0.5
28 Oct 03:05:46	80	56–58	346–347	97.4 ± 1.2	792	>16	1.9	9.0	3.02	1.6
29 Oct 01:14:34	1060	66–86	22–36	87.1 ± 2.6	444	5.3	2.0	4.6	0.57	0.6
23 Nov 21:42:38	750	52–61	269–283	92.0 ± 2.3	200	4.9	2.0	6.2	0.58	0.4
23 Nov 23:14:42	1660	39–57	57–78	73.3 ± 5.9	257	3.9	2.5	5.7*	0.22*	0.2
24 Nov 04:11:14	560	57–62	176–193	85.7 ± 1.0	943	7.1	1.3	4.1	0.85	1.0
4 Dec 04:36:58	260	78–85	169–179	91.2 ± 0.9	359	11.6	1.8	5.9	2.31	1.8
5 Dec 03:31:18	590	72–83	128–196	87.5 ± 1.1	339	>16	1.9	4.8	1.87	1.8
8 Dec 02:33:23	750	60–65	171–215	92.1 ± 0.6	456	>16	3.0	7.5	8.01	5.0
12 Dec 17:29:43	950	59–71	164–204	81.2 ± 1.9	674	11.2	1.9	3.6	2.29	3.0
12 Dec 18:21:07	1120	39–57	220–233	86.9 ± 6.7	471	>16	2.3	4.3	11.64	12.9
13 Dec 20:28:48	990	57–60	164–191	93.4 ± 0.5	130	5.1	2.2	5.6	0.35	0.3
14 Dec 14:00:46	1460	41–62	223–243	89.3 ± 7.8	77	4.7	4.2	5.1	0.23	0.2
14 Dec 15:20:41	430	83–88	55–169	87.1 ± 0.4	200	5.8	3.5	4.3	0.57	0.6
16 Dec 23:08:40	460	53–55	69–77	85.1 ± 0.9	798	>16	2.4	3.9	2.75	3.3
17 Dec 02:41:38	720	59–80	31–67	96.1 ± 3.9	206	>16	5.2	8.6	4.51	2.5
22 Dec 18:43:52	690	49–65	151–175	88.5 ± 4.8	129	11.2	3.8	5.0	2.32	2.2
22 Dec 21:17:36	410	66–76	171–204	94.8 ± 1.3	144	11.3	3.3	8.4	6.59	3.7
22 Dec 23:25:04	110	51–52	277–278	97.2 ± 1.1	58	>16	4.1	9.0	1.35	0.7
23 Dec 00:55:38	460	58–69	-1-1	95.4 ± 2.3	204	>16	4.1	7.7	9.87	6.0
27 Dec 02:54:14	160	84–86	161–191	84.4 ± 0.1	285	11.1	2.3	4.1	4.89	5.6
27 Dec 05:09:29	160	79–80	282–287	93.7 ± 0.1	271	6.0	2.8	8.5	1.74	1.0
28 Dec 18:13:46	260	40–43	258–258	79.1 ± 1.8	610	4.0	1.4	3.9	0.16	0.2

*Diffusion coefficient is not reliable below 80 km and above 100 km.

ionosonde meteor traces are accompanied by MC detections. First, MC detections during daylight or cloudiness are limited to very rare bolide or superbolide events bright enough to outshine the sky background, whereas light and cloud conditions do not affect ionosonde observations. Second, many meteors producing ionization may not be bright enough to be detected by the meteor camera.

On the other hand, some meteors observed optically do not appear in the ionosonde data. In particular, this may be caused by radio waves absorption (e.g., between 0730 and 1230 UT on 12 December 2015, Figure 2) or when specular reflection is not possible, for example, if a meteoroid trajectory is radially aligned toward the ionosonde. Also, meteor trails may be hidden during enhanced ionization caused by electron precipitation, for example, near 20 UT on 12 December 2015 (Figure 2).

Using FTI plots and also individual ionograms, we carefully inspected all 317 cases of MC detection during the year 2015 and selected those cases for which the corresponding meteor traces were clearly identified as isolated events in the ionosonde data. This corresponds to echoes of the first type according to Ellyett and Goldsbrough (1976) and Maruyama et al. (2003). We note that during intense meteor showers several ionized trails may overlap (the second type echo occurs), such that one-to-one identification of optical meteors and their effects in the ionosonde data sometimes is impossible. For instance, there were three MC detections between 20 and 21 UT on 12 December 2015, and there are many signatures of meteors in the FTI plot during this time (Figure 2), but we are not able to identify for certain the effects of individual meteors. Thus, although the MC detected 14 meteors on this day, only two meteor events, namely, at 1729 and 1821 UT, were selected for further analysis.

Altogether, 28 cases were selected. They are listed in Table 1, where data under heading "Meteor camera" are date and time (UT) of detection, duration of luminosity (ms), and intervals of the elevation and azimuth
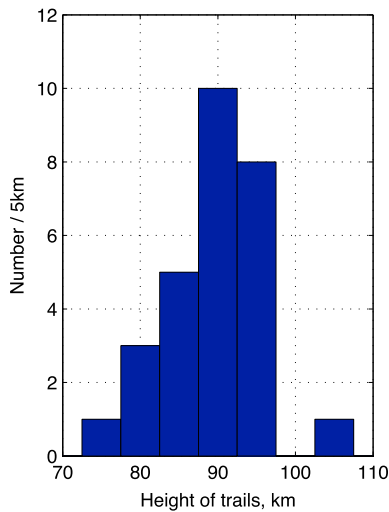
Figure 4. Height distribution of the ionosonde detections of meteor trails.

angles (degrees) at which the traces were observed. The majority of the events occurred in December, in particular during the Geminid meteor shower, which has a broad activity maximum between 27 November and 18 December and in 2015 peaked on 14 December (Jenniskens, 2006). The flux of sporadic meteors is also significant in the Northern Hemisphere at this time (Fentzke et al., 2009).

4. Height of Meteor Trails

The ionograms obtained just after detection of a meteor were used to measure the distance from the ionosonde to the ionization trail. The distance is determined as a virtual height of the low edge of the Em trace. After that, taking into account direction (azimuth and elevation angles) toward the meteor from the camera, we calculated the position (height, latitude, and longitude) of the trail.

Heights of the trails are given in the fifth column in Table 1 together with the uncertainty values representing the extent of the optical traces of the meteors. In most cases this uncertainty does not exceed 2 km. However, one should also take into account the uncertainty of the distance measurement, which is 3 km at least. Indeed, the spatial resolution of SGO ionograms is 2.86 km and, moreover, traces at ionograms are sometimes not distinct. Thus, the main errors in the location of meteor trails arise from the measurements of virtual height in ionograms rather than from the extent of the optical meteor traces. In total, the height uncertainty may be a few kilometers.

The histogram in Figure 4 shows the height distribution of the ionized meteor trails. A great majority of the trails are located between 80 and 100 km with a sharp maximum of occurrence around 90 km. This agrees very well with the averaged height distribution of meteor echoes obtained from the whole period of the SGO meteor radar observations (Lukianova et al., 2017).

5. Duration of Meteor Echoes

Figure 5 shows an enlarged FTI plot for the meteor event at 17:29:43 UT on 12 December 2015. During the ionosonde sounding performed immediately after the meteor event, radio waves at frequencies up to about 11 MHz were backscattered from distances between 80 and 130 km (a more precise value obtained from the ionogram is 90.5 km). In subsequent soundings performed during the following 11 min, the maximal backscattered frequency systematically decreased down to a background level of the order of 2 MHz. Such a decrease of the maximal backscattered frequency was observed in all the 28 selected cases of the first type
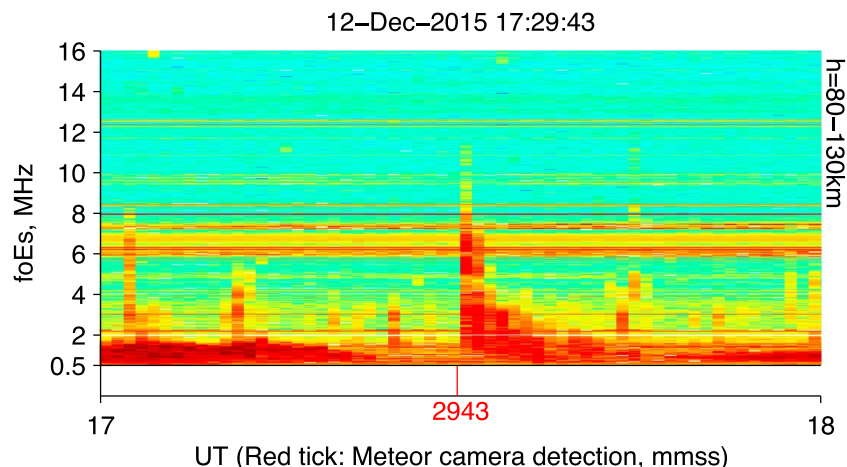

Figure 5. Enlarged FTI plot for the meteor event at 17:29:43 UT on 12 December 2015.
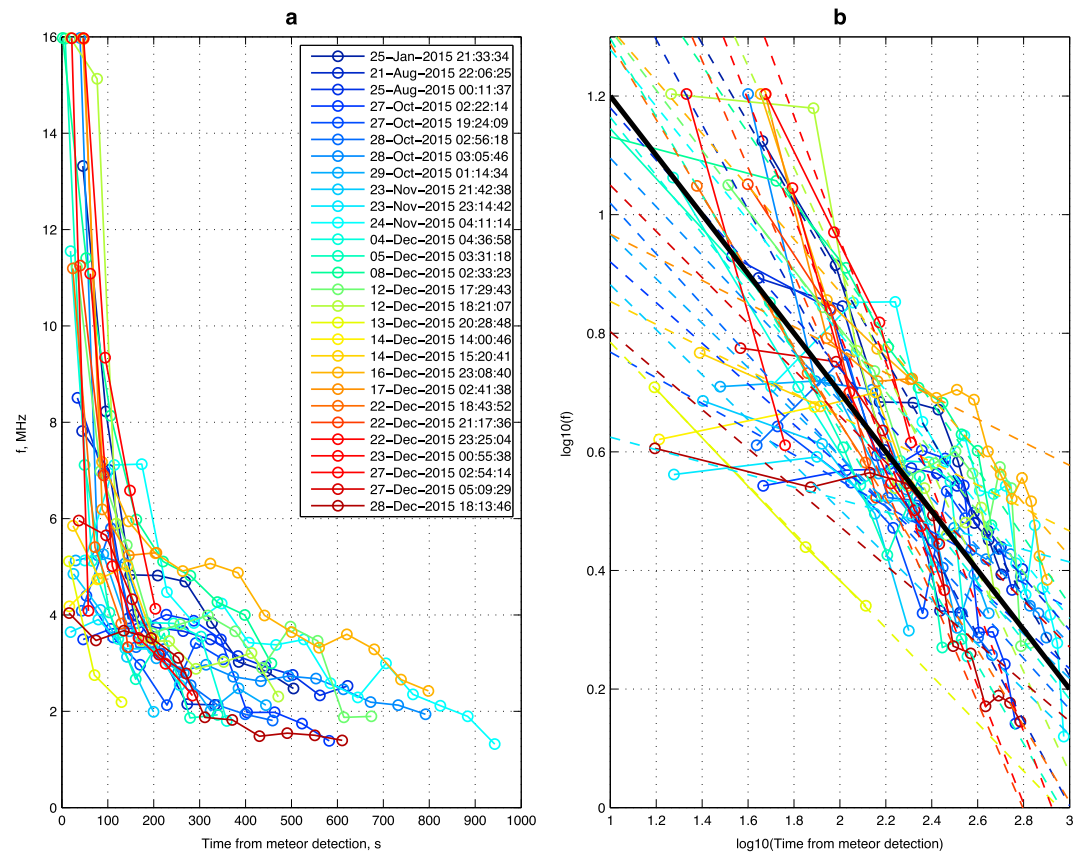
Figure 6. Dependence of the maximal backscattered frequency on the time from meteor detection for the selected 28 events (different colors correspond to different meteor events according to the legend): (a) linear scale and (b) logarithmic scale. Dashed lines of corresponding colors show approximations of the 28 experimental curves $\log_{10} f$ against $\log_{10} \tau$ by a least squares linear fit.

echoes. This means that the duration of reflection (τ) at certain frequency of transmission (f) decreases with the frequency of transmission. In the following we check to which extent this dependence agrees with quation (2).

Curves in Figure 6a show the dependence of the maximal backscattered frequency on the time from meteor detection for the selected 28 events. Different colors correspond to different meteor events according to the legend. The frequency was measured from the ionograms, which allows better accuracy than FTI plots. Although the ionosonde sounding is made once a minute, the time of transmission at a certain frequency is determined with much better accuracy. Indeed, the ionosonde starts transmitting 5 s before every integer minute and the frequency of transmission is increasing from 0.5 to 16 MHz at a rate of 0.5 MHz/s. Typically, the uncertainty of the maximal received frequency obtained from ionograms is of the order of 0.5 MHz, so that the time accuracy is about 1 s. The duration (t_i) of Em in the ionosonde data since MC detection and frequency range of $foEm$ (from f_{max} to f_{min}) are given in Table 1 under heading "Ionosonde." In the cases when echoes were received at frequencies up to the upper limit (16 MHz) we were unable to determine a maximal received frequency and therefore assigned a value of 16 MHz.

The vertical axis in Figure 6a shows the maximal backscattered frequency, and horizontal axis shows time of the echo at this frequency. Zero time corresponds to the moment when the meteor camera detected the meteor. If the trails are overdense and equation (2) is valid, curves in Figure 6a should satisfy the power law

$$f \propto \tau^{-\gamma} \tag{4}$$

with an exponent $\gamma = 0.5$. For testing whether this is the case, Figure 6b presents data from Figure 6a in a logarithmic scale. Dashed lines of corresponding colors show approximations of the 28 experimental
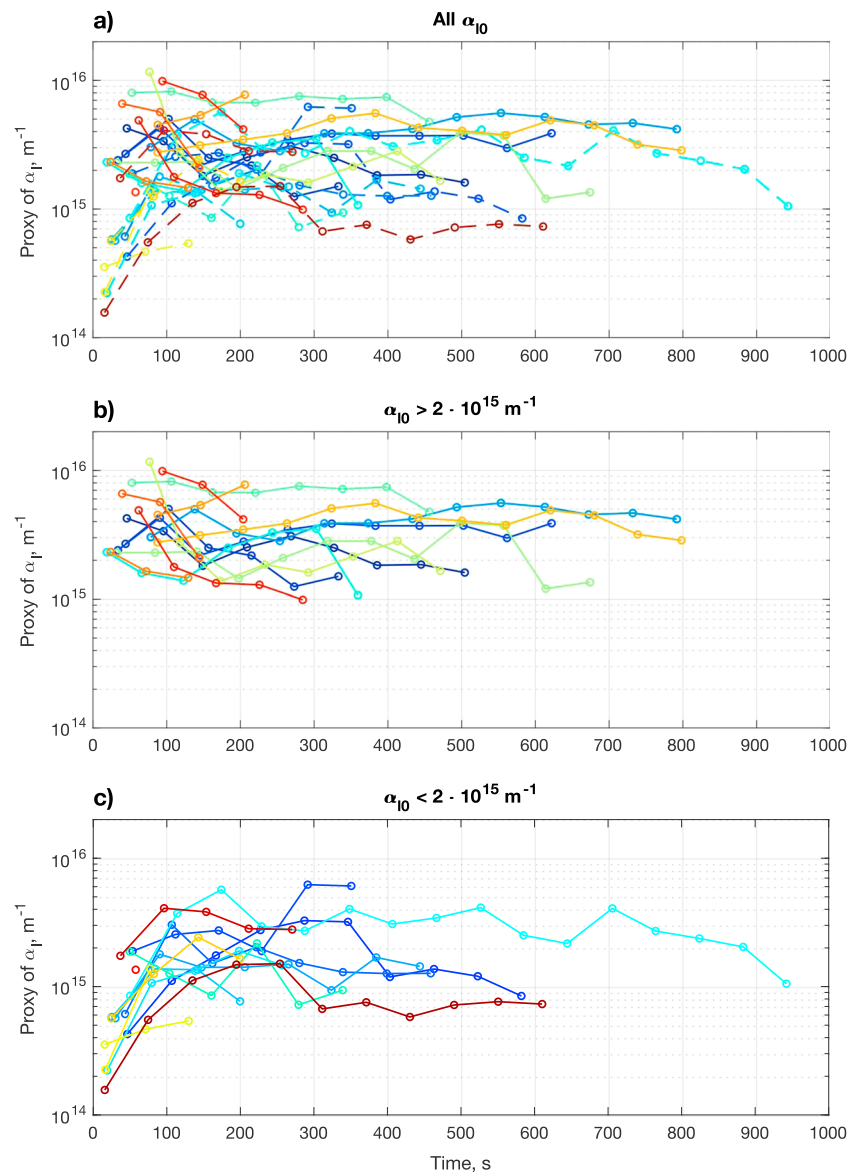
Figure 7. Electron line density of meteor trails versus time since the moment of the meteor camera detection. Colors of the curves indicate date and time of the meteor events according to the legend in Figure 6: (a) all trails. Full and dashed curves indicate data of trails, which α_{l0} are larger and less than $2 \cdot 10^{15}$ m^{-1}, respectively; (b) data of trails, which α_{l0} are larger than $2 \cdot 10^{15}$ m^{-1}; and (c) data of trails, which α_{l0} are less than $2 \cdot 10^{15}$ m^{-1}.

curves $\log_{10} f$ against $\log_{10} \tau$ by a least squares linear fit (where data points at frequencies exceeding 16 MHz were not taken into account). On average, the slope of the lines is -0.506 ± 0.123 (i.e., $\gamma \approx 0.5$), which seems to favor overdense trails and thus validate equation (2) on a timescale of the order of 10 min. However, a more careful analysis below shows that this issue is more complex.

6. Electron Line Density of Meteor Trails

Above we have utilized data from the ionosonde and the meteor camera to obtain the duration (τ) of echoes from meteor trails at certain backscattered frequencies (f) and height (H) of the trails. Diffusion coefficients (D) at the time and height of these meteor trails are given in Table 1. The diffusion coefficients were obtained from the meteor radar observations of underdense meteor trails, which is described below in section 7. The typical uncertainty in the diffusion coefficients is on the order of 2–3 m^2/s. Thus, we have all necessary
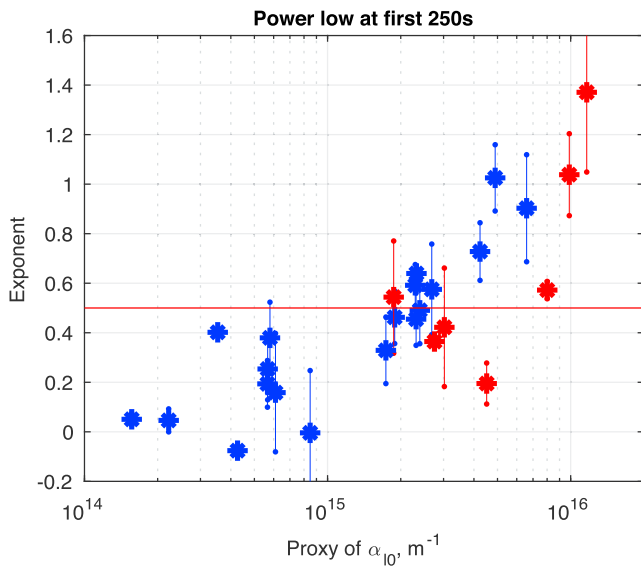
Figure 8. Exponent γ in equation (4) calculated for each individual meteor during its first 250 s versus the proxy of initial density (α_{l0}) of the trails. Horizontal red line indicates the exponent $\gamma = 0.5$, which corresponds to the diffusional expansion of cylinder-like overdense trails.

data for calculating the electron line density of the trails (α_l) according to equation (2). The density of a trail can be calculated independently from several (up to 15) ionograms in which the trail was identified at different f and τ, so that several values of α_l can be obtained for one trail.

Figure 7 presents the line density of all trails calculated at different times. The horizontal axis indicates the time, and zero time is the moment of meteor detection by the meteor camera. Colors of the curves indicate date and time of the meteor events according to the legend in Figure 6a. If equation (2) is valid, the calculated values of line density for each trail should be about the same independent of time. However, Figure 7 shows systematic temporal changes of α_l during the first 250 s. The character of the changes depends on the value of line density calculated in the very beginning of the event (denoted below as α_{l0}). Namely, the calculated density of trails increases with time if $\alpha_{l0} < 2 \cdot 10^{15}$ m^{-1} and tends to decrease if $\alpha_{l0} > 2 \cdot 10^{15}$ m^{-1}. To illustrate this feature, full and dashed curves in Figure 7a indicate data of trails where α_{l0} are larger and less than $2 \cdot 10^{15}$ m^{-1}, and additionally, these data are shown separately in Figures 7b and 7c, respectively. Values of α_{l0} for all the events are given in Table 1.

The data in Figure 7 suggest that during the first 250 s, the evolution of the meteor trails does not follow equation (2). Hence, the calculated values of α_l may differ from the true electron line density of meteor trails. We are therefore considering them only as a proxy of the density. Nevertheless, these values are reasonable in the order of magnitude corresponding to overdense or transitionally dense trails, which are further referred as nonunderdense trails.

To understand the evolution of meteor trails, we calculated the exponent γ in equation (4) for each individual meteor during the first 250 s of each event. These values are presented in Figure 8 plotted against the proxy of initial density (α_{l0}) of the trails. For the data points indicated in blue, α_{l0} was obtained during the first minute (from the first ionogram) after the optical meteor was observed. Red color indicates that the 16-MHz frequency limit was exceeded in the first ionogram. For these cases α_{l0} was obtained during the subsequent minute.

The horizontal red line in Figure 8 indicates the exponent $\gamma = 0.5$, which corresponds to the diffusional expansion of overdense trails according to equation (2). This plot demonstrates that the exponent decreases against the initial linear density of trails, namely,

1. for $\alpha_{l0} < 10^{15}$ m^{-1} (corresponding to transitionally dense trails) the exponent value is smaller than 0.5 (of the order of 0.2), which means slower than diffusional decay of meteor trails;
2. for $\alpha_{l0} \sim (2–3) \cdot 10^{15}$ m^{-1} $\gamma \approx 0.5$, which agrees with diffusional expansion of overdense trails;
3. for $\alpha_{l0} > 5 \cdot 10^{15}$ m^{-1} $\gamma > 0.5$ (of the order of 1), which indicates fast decay of electron density in the trails.

We summarize this finding as

$$\gamma \in \begin{cases} < 0.5 \text{ if } \alpha_{l0} < 10^{15} \text{m}^{-1} \\ \approx 0.5 \text{ if } \alpha_{l0} \in (2 - 3) \cdot 10^{15} \text{m}^{-1} \\ > 0.5 \text{ if } \alpha_{l0} < 5 \cdot 10^{15} \text{m}^{-1} \end{cases} . \tag{5}$$

Possible reasons for this dependence are discussed in section 8.

7. Meteor Radar Observations

The SGO meteor radar (MR) is an all-sky interferometric meteor radar (SKiYMET), which transmits short bursts (pulses) of very high frequency ($f_{MR} = 36.9$ MHz) radio waves. The transmit antenna has a broad radiation pattern designed to illuminate a large expanse of the sky. Processing software on the MR analyzes the returned

signals and selects only those signals, which are believed to be echoes from meteor trails. The characteristic features used to distinguish meteor echoes from other signals include their rapid onset, relatively short duration (typically less than 2 s), and quasi-exponential decay. The majority of meteor trails are underdense, and moreover, the detection algorithm may reject overdense trails as nonmeteor signals (Hocking et al., 2001). Nevertheless, some SKiYMET meteor radar detections lasting a few tenths of a second are from overdense trails (Kozlovsky et al., 2016).

The receiving system determines the azimuth, elevation, range, height, and Doppler velocity of the selected targets. For each detection identified as a meteor echo the decay time, that is, the half-lifetime, $\tau_{1/2}$, defined as when the amplitude of the received signal has decreased by half, is calculated from the width of the autocorrelation function of the received signal.

According to equation (2), the diffusion coefficient can be calculated from the half-lifetime of underdense meteor trails as

$$D = \frac{\lambda^2 \ln 2}{16\pi^2 \tau_{1/2}} \qquad (6)$$

The diffusion coefficients presented in Table 1 are daily averaged values calculated from the half-lifetime of all meteor trails detected at a given height within a 2-km layer. The majority of the meteors is detected in a height range between 80 and 100 km. This means that the diffusion rate data below and above this layer (at 2314 UT on 23 November and 1924 UT on 27 October, respectively) are not reliable. The diffusion coefficients obtained from MR data were used to calculate the electron line density of the meteor trails as described in section 6 above.

Using equation (2), we estimate the expected duration τ_{MR} of MR echoes from the meteor trails according to

$$\tau_{MR} = \tau_{iono1} \frac{f_{iono1}^2}{f_{MR}^2} \qquad (7)$$

where f_{iono1} is the maximal frequency of the first ionosonde echo after the optical detections of meteors and the duration τ_{iono1} is counted since the onset of optical meteors (in the cases when the first echoes were received at frequencies up to the upper limit of 16 MHz we used f_{iono2} and τ_{iono2} corresponding to the second ionograms after the optical meteors). The expected duration of MR echoes is typically a few seconds or less, which is given in the last column in Table 1. The overdense echoes that lasted longer than few tenths of a second are to be rejected by the MR detection algorithm as nonmeteor targets. Nevertheless, next we consider the meteor radar detections obtained simultaneously (within a few seconds) with the optical detections of meteors.

7.1. Examples of Meteor Radar Detections

Figure 9a shows a map of the region of observations. Horizontal and vertical axes show distances (km) to north and east from the location of the SGO ionosonde and meteor radar. A circle to the northwest of SGO indicates the position of the meteor camera. The line directed to SGO from southwest represents a meteor trace (mapped to the Earth surface), the location of which was calculated from the data of meteor camera data (azimuth and elevation) and ionosonde range on 5 December at 0331 UT. Dots along the line correspond to the sequence of meteor locations (through ~40 ms), and the largest dot near SGO shows the last location.

Numbered red asterisks show positions of five targets detected by the meteor radar during the optical meteor (within a few seconds). Heights of the detected targets are given in the parentheses. One can see that the MR targets are located along the optical meteor trace at heights descending from 102 to 92 km. Hence, the meteor trajectory was aligned from the southwest toward zenith above SGO at an angle of about 65° to vertical. Obviously, the condition of specular reflection (i.e., 90° angle between the meteor trajectory and the meteor radar beam) was not satisfied in this case.

Figure 9b shows positions of the optical meteor and the meteor radar detections for the event on 14 December at 1520 UT. In this case five meteor radar targets and the optical meteor trace are located along
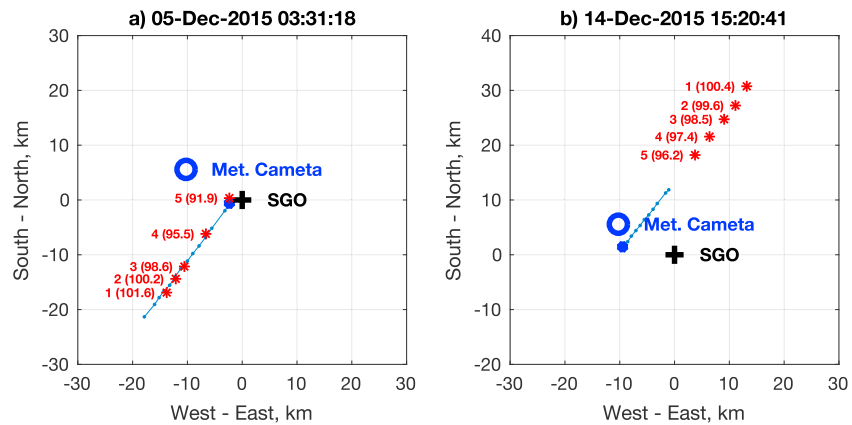
Figure 9. Maps of the region of observations (a) on 5 December at 0331 UT and (b) on 14 December at 1520 UT. A circle in the northwest of SGO indicates position of the meteor camera. The blue lines represent the meteor traces (mapped to the Earth surface). Dots along the lines correspond to the sequence of meteor locations (determined each ~40 ms from individual video frames). The largest dots near SGO show the last locations. Numbered red asterisks show positions of five targets detected by the meteor radar during the optical meteor. Heights of the detected targets are given in the parentheses.

same line, however, at different parts of the trajectory and therefore also at different heights. The MR targets are at heights descending from 100 to 96 km, and simple geometry shows that the optical meteor was observed at heights between 90 and 95 km.

For all the MR detections identified as meteors, short 4-s records of the amplitude and phase of the received signals at one range gate are archived. Figure 10 presents such a record of the signal corresponding to the detection number 4 on 5 December at 0331 UT (Figure 9a). In this plot the amplitude of the signal received at one of the five MR antennas is presented versus time. Zero time approximately corresponds to the time of meteor radar detection. One can see that the signal is highly variable. The echo lasted longer than 3 s, which is longer than the lifetime of 1.8 s as estimated using the ionosonde data.

Unfortunately, the streamed raw data are not stored completely in the meteor radar database. Figure 11 shows all stored data (i.e., the 4-s records) during the two events, on 5 December at 0331 UT (a) and on 14 December at 1520 UT (b), in range-time-intensity plots (RTI). Earlier, Schult et al. (2015) used such an RTI plot for presenting MR data during the Maribo fireball event on 17 January 2009. Comparison of their data with the RTI plots in Figure 11 reveals common features of the events. In particular, detections in the upper range gates from 102 to 106 km on 14 December (Figure 11b) are "weak nonspecular trails," whereas detections in the ranges from 92 to 100 km on 5 December (Figure 11a) and at 98 km on 14 December look like "saturated trails" according to the nomenclature used by Schult et al. (2015).
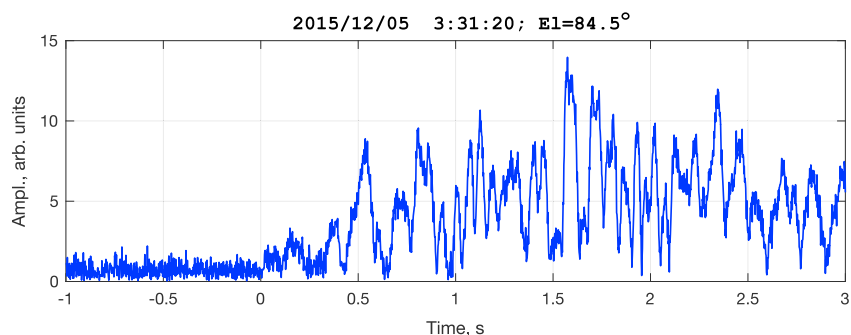

Figure 10. Record of the amplitude received at one of the meteor radar antennas, corresponding to the fourth detection on 5 December 0331 UT illustrated in Figure 9a. Zero time approximately corresponds to the time of meteor detection.
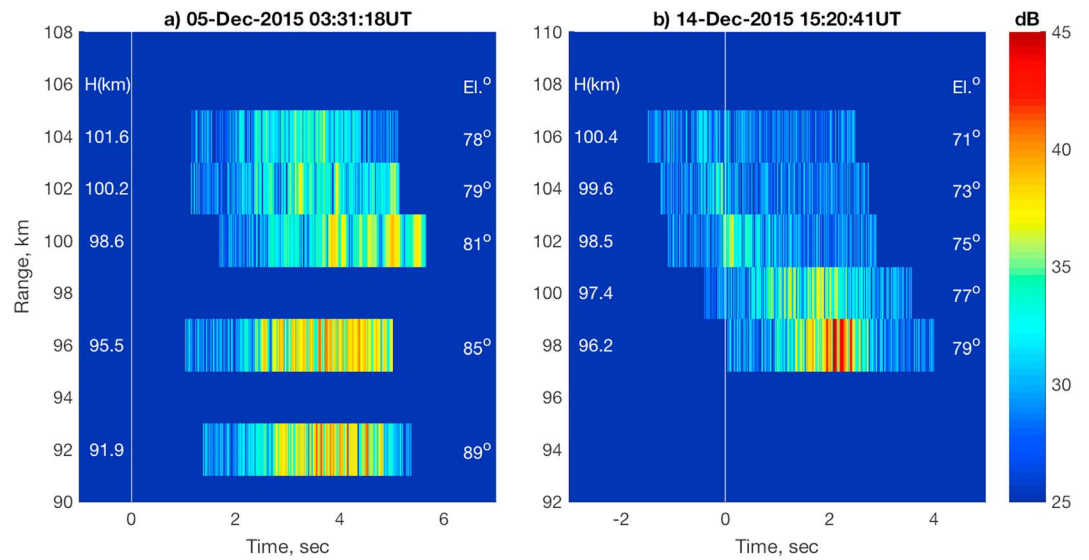
Figure 11. Range-time-intensity plots during the events (a) on 5 December at 0331 UT and (b) on 14 December at 1520 UT. Heights and elevation angles of detections are indicated on the right and left of the plots, respectively. Zero time corresponds to the moments of optical meteors detections.

Further, although the RTI plots are fragmented because of incomplete data sets, they well correspond to the range-time-intensity measurements of nonspecular long-lived radar echoes presented by Chau et al. (2014). Their observations were made at high latitudes (about same as SGO) and obviously were associated with large enough meteoroids.

7.2. Characteristics of Meteor Radar Echoes

We use the same analysis procedure of the meteor radar data for all the events listed in Table 1. In 16 of the 28 cases the meteor radar located from one to five targets in the same time and place when and where the meteor camera detected a meteor trace. These data are summarized in Table 2, where date and time of the meteor observations and the heights obtained from ionosonde (repeating Table 1) are given on the left. Then, parameters of the meteor radar detections (height, elevation, and duration of the echoes) are presented.

Looking through the maps of meteor locations (such as Figure 9), we conclude that the condition of specular reflection could not be satisfied in the cases when elevation angles of targets were larger than about 80°. This is shown by simple geometry. Thus, at least about half of the MR detections were nonspecular.

The duration of the echoes was determined from the 4-s amplitude records of the received signals. In the cases when the end of the signal was not recorded in the 4-s record, its duration is indicated as ">3." As a rule, the signals were long lasting and variable, as in the example shown in Figure 10. Their duration is typically longer than that estimated by equation (7) from the ionosonde data (the latter, $\tau_{MR}(\tau_{iono})$, is repeated from Table 1). However, with a few exceptions, the meteor radar typically detected the targets about 10 km higher than the ionosonde did. With taking into account the electron line density estimated above (in the last right column α_{l0} is repeated from Table 1) and the diffusion coefficients corresponding to the heights of MR detections, we recalculated the expected durations of MR echoes according to equation (2). If the height was above 100 km, we give an upper limit estimation using a diffusion coefficient corresponding to the 100-km height. The obtained values are indicated as $\tau_{MR}(\alpha_{l0}, h_{MR})$ in Table 2 for comparison with the observed durations of echoes. The comparison shows that in many cases meteor events were accompanied by long-lived radar detections (indicated by ** in Table 2). These detections have a duration noticeably longer than that expected from the diffusional expansion of cylindrical meteor trails estimated using equation (2).

Table 2
Data of Meteors From Meteor Radar Observations

Date and time	H_iono (km)	Heights MR	El. (deg.)	Duration	τ_{MR} (α_{l0}, h_{MR})	τ_{MR} (τ_{iono})	α_{l0}, 10^{15} el/m
25 Aug 00:11:37	92.1	92.3	70.2	>3[a]	1.8	1.8	2.40
27 Oct 19:24:09	105.9	103.3	60.9	0.3	<1.0[b]	0.8	1.89[b]
28 Oct 02:56:18	89.6	102.6	80.5	1.5[a]	<0.3	0.5	0.61
29 Oct 01:14:34	87.5	98.8	81.2	1.5[a]	0.3	0.5	0.57
		96.7	80.9	>3[a]	0.3		
		79.2	67.0	1.0	0.7		
23 Nov 23:14:42	73.6	94.8	61.6	>3[a]	0.1[b]	0.2	0.22[b]
		83.2	56.1	0.3	0.3[b]		
4 Dec 04:36:58	91.3	106.8	81.5	1.0	<1.2	1.8	2.31
		103.2	82.9	>3[a]	<1.2		
5 Dec 03:31:18	87.8	101.6	77.7	2.5[a]	<0.8	1.8	1.87
		100.2	79.2	>3[a]	<0.8		
		98.6	80.6	>3[a]	1.0		
		95.5	84.5	>3[a]	1.1		
		91.9	88.5	2.5[a]	1.3		
12 Dec 17:29:43	81.6	98.7	75.4	1.5	1.2	3.0	2.29
		96.3	74.4	3.0	1.4		
14 Dec 14:00:46	89.9	98.8	59.8	>3[a]	0.1	0.2	0.23
		94.1	51.3	>3[a]	0.2		
14 Dec 15:20:41	87.2	100.4	71.3	0.2	<0.3	0.6	0.57
		99.6	73.3	0.3	0.3		
		98.5	74.8	1.0	0.3		
		97.4	76.8	2.0[a]	0.3		
		96.2	78.9	1.8[a]	0.4		
22 Dec 18:43:52	88.9	93.2	49.5	2.8	1.5	2.2	2.32
22 Dec 21:17:36	95.0	110.8	81.5	0.3	<3.2	3.7	6.59
		108.4	80.2	0.5	<3.2		
		103.8	73.9	>3	<3.2		
22 Dec 23:25:04	97.2	110.9	58.3	0.5	<0.6	0.7	1.35
23 Dec 00:55:38	95.6	103.3	62.8	>3	4.4	6.0	9.87
27 Dec 02:54:14	84.3	92.5	79.8	3	3.1	5.6	4.89
		90.9	81.8	>3	3.5		
28 Dec 18:13:46	79.1	101.4	62.6	0.4[a]	<0.1	0.2	0.16
		100.2	59.6	0.5[a]	<0.1		
		98.7	55.0	2.3[a]	0.1		
		96.7	50.9	>3[a]	0.1		

[a]Long-lived meteor echoes.   [b]Diffusion coefficient is not reliable below 80 km and above 100 km.

8. Discussion

The present study is devoted to meteors, which are bright enough to be automatically captured in the video stream from a wide-angle meteor camera. Such meteors produce relatively dense (nonunderdense) ionization trails. To investigate the ionization trails, we use radar sensing in two essentially different frequency bands, namely, 36.9 MHz (meteor radar) and 0.5–16 MHz (ionosonde). This allows monitoring of the trail development at two different timescales, a few seconds and several minutes, respectively.

8.1. Ionosonde Observations

As a good approximation, overdense meteor trails are usually described as cylinders of enhanced ionization expanded due to diffusion, in which case the duration of radio echoes is given by equation (2). In the present study we have obtained that on average the decay of trails in the ionosonde data follows equation (2), but during the first 250 s the decay rate depends on the line density of the trails.

Earlier, Maruyama et al. (2003) performed similar rapid-run ionosonde observations of meteors during the Leonid meteor shower and analyzed in details the decay of one overdense meteor trail. They had no collocated meteor camera data for exact timing and location of the meteor and no data of the diffusion rate,

and instead, reasonable assumptions were used for numerical estimations. For the trail with presumed line density 10^{17} m^{-1} Maruyama et al. (2003) obtained that neither recombination nor diffusion could explain the decay of the trail, but except the first 3 min, the decay follows an exponential law, which nature is unknown. It is difficult to compare the observation of Maruyama et al. (2003) with data of the present paper because in their case the trail line density was 1 to 3 orders of magnitude larger than that in our events. However, it is remarkable that Maruyama et al. (2003) also noticed different characters of the decay during the first 3 min and later.

One more factor that may affect the lifetime of meteor trails is the wind shear deformation of the trails (Maruyama et al., 2003). This mechanism was used to explain the long-duration (40 min) meteor echo in the rapid-run ionosonde observations during the Perseid meteor shower (Maruyama et al., 2008). In fact, this mechanism implies transformation of the dense meteor trail into a sporadic E patch generated from meteor trail plasma. Such a process requires some time, which means that the effect may become noticeable only at the last stage of the meteor trail evolution. In the present study we followed the decay of the meteor trail's ionization down to slightly above the background electron density. However, at high latitudes the ionosphere is highly variable due to electron precipitation, which contaminates ionosonde detection of the meteor trails when their electron density is close to the background. This is likely a reason for which we did not detect such long-duration echoes as Maruyama et al. (2003, 2008) observed at middle and low latitudes.

An important factor to note is that the presence of the meteoric dust originating from ablation of large meteoroids decreases the diffusion rate, so that the lifetime of meteor trails is extended as it follows from the quantitative analysis of ionosonde data (Shalimov & Kozlovsky, 2015). Effectively, this would manifest itself as a smaller than 0.5 exponent in equation (4). This may explain the exponent values smaller than 0.5 (of the order of 0.2) for $\alpha_{l0} < 10^{15}$ m^{-1} (corresponding to transitionally dense trails) in equation (5). For more dense trails (larger α_{l0}), recombination can play a noticeable role in addition to the diffusion. As the recombination rate is proportional to the square of volume electron density (n^2), the decay rate of more dense trails is larger, which means that the value of γ is larger. Thus, the dependence shown in Figure 8 and expressed by equation (5) may be qualitatively explained by the competition of two mechanisms: the presence of meteoric dust decreasing the rate of diffusion and recombination increasing the decay rate of the more dense meteor trails. Meteor smoke particles of about 1 nm in size exist at the heights around 90 km, and their concentration may be on the order of 10^2–10^4 per cubic centimeter depending on the season (Fentzke et al., 2009). In the subsequent studies these hypotheses are to be checked quantitatively with taking into account chemical reactions and other processes like turbulent diffusion, attachment, and neutral winds, but such theoretical analysis is out the scope of the present experimental study.

8.2. Meteor Radar Echoes

It has long been believed that equation (2) is valid only for times less than 10 s, as for longer timescales, recombination, attachment, turbulent diffusion, and other processes should play important roles in the decay of meteor trails (e.g., Bronshten, 1983). Our results presented in section 7 show that even at timescales less than 10 s, the behavior of overdense meteor trails can be more complex than just a diffusional expansion. It appears that long-lived highly variable irregularities of electron density are formed along the traces of bright meteors, so that the meteor radar detects nonspecular reflections from them. At low and middle latitudes nonspecular meteor echoes can originate from magnetic-field-aligned irregularities of electron density (e.g., Dyrud et al., 2011; Oppenheim et al., 2003), but it is impossible at the high-latitude SGO site where the magnetic field lines are closer to the vertical.

To explain nonspecular long-lived echoes from meteor trails at high latitudes, another possible mechanism was suggested by Chau et al. (2014). Their observations are very similar to our ones, and we cite: "…echoes could be qualitatively explained by the presence of charged dust forming from the meteoric material immersed in a turbulent flow. This can lead to a high Schmidt number plasma that can sustain meter-scale turbulence just as it does for the polar mesospheric summer echoes. These rare events require relatively large meteoroids." We have shown that the nonspecular meteor echoes are indeed generated along trails of bright meteors, and we have estimated the electron line density of the trails. These quantitative data may be useful for future theoretical and modeling studies to understand nature of the phenomena.

In distinction from the ionosonde receiving Fresnel echo from patches of enhanced electron density, the meteor radar echoes in this case are Bragg backscatter from the meter-scale irregularities formed along the meteor trajectory. Chau et al. (2014) suggested that such irregularities are formed due to turbulence of the neutral atmosphere, whereas dust particles are only responsible for slower diffusion. However, dust particles may play an important role in generating meter-scale irregularities as well. Trakhtengerts (1994) suggested that the mesosphere summer echoes can be generated due to the instability in which aerosol ice particles play a key role. Sedimented by gravity and, hence, moving with respect to the background plasma, charged aerosol particles can produce meter-scale irregularities (electrostatic waves) via a dissipative instability, a mechanism which is analogous to that of the resistive beam-plasma instability. This mechanism does not require a hypothesis of atmospheric turbulence and is solely based on the presence of aerosols.

Kozlovsky et al. (2017) adopted the model of Trakhtengerts (1994) to explain meteor radar echoes from the mesospheric plasma irregularities caused by the missile destruction in December 2009. Instead of ice aerosols, Kozlovsky et al. (2017)considered 100-nm aluminum oxide particles from the solid rocket propellant and obtained that this mechanism could produce the highly variable MR echoes, which were very similar to that shown in Figure 10. Obviously, 1-nm meteor smoke particles (MSPs) are too light for getting essential velocity of sedimentation. However, neutral wind may drag the MSP with respect to the background free electrons, so that the instability may develop. In such a case the model will be much more complex because the magnetic field must be taken into account. We intend to investigate this problem theoretically in a subsequent paper.

Thus, presence of dust particles may be responsible for both the slower decay of the meteor trails observed by ionosonde and the long-duration nonspecular meteor echoes detected by the meteor radar.

9. Summary

Using 1 year of data from the SGO meteor camera observations, we found and investigated 28 optical meteors with accompanying ionization trails unambiguously detected by the SGO ionosonde performing 1-min sounding with linearly rising frequency from 0.5 to 16 MHz. These ionosonde reflections were obtained from heights around 90 km. Values of the electron line density of the trails were found to be in the range between 10^{14} and 10^{16} m^{-1}, which characterize the trails as nonunderdense (i.e., transitional and overdense).

The ionosonde reflections from the trails were observed during a few (up to about 12) minutes and the maximal frequency of the return signals decreased with time. We have found that during the first 250 s the decay rate of the trails depends on their line density. For the trails with initial line density about $(2-3) \cdot 10^{15}$ m^{-1} the frequency decrease rate corresponds to diffusional expansion of cylindrical meteor trails ($f \propto t^{-\gamma}$, $\gamma = 0.5$), whereas less dense trails decayed slower ($\gamma \approx 0.2$) and more dense trails decayed faster ($\gamma \approx 1$). We consider this as the most important and novel result and suggest that probably, this dependence might be qualitatively explained by a competition of two mechanisms: the presence of meteoric dust leading to a decrease of the diffusion rate and recombination leading to increased rate of decay for the more dense meteor trails.

In addition, we considered simultaneous data from the SGO meteor radar operating at a frequency of 36.9 MHz, which allows monitoring the evolution of the meteor ionization at a timescale of a fraction to a few seconds. In many cases the meteor events were accompanied by long-lived meteor radar detections, which duration is longer than that expected from diffusional expansion of cylindrical meteor trails. Many of the meteor radar detections were nonspecular. Similar observations have been reported by Chau et al. (2014), who suggested that nonspecular long-lived echoes from meteor trails could be explained by the presence of charged dust forming from the meteoric material immersed in a turbulent flow.

Thus, two observational results of this study, the slow frequency decrease of ionosonde echoes and the nonspecular long-lived meteor radar echoes, may be associated with the presence of meteoric dust.

Finally, we list the main open issues, which arise from the present experimental study and which will need subsequent investigations:

1. The dependence of the decay rate of ionosonde echoes on the initial electron line density of the trails (empirical dependence illustrated in Figure 8) needs to be explained quantitatively.
2. The generation of long-duration nonspecular meteor echoes along trajectories of large meteoroids and the role of meteoric dust particles needs to be understood theoretically.

3. Because of limitations in the optical observations, the data were obtained mostly in December during the Geminid meteor shower. For improving statistics and accounting the role of shower and sporadic meteoroids multi-instrumental observations need to be continued.

References

Bronshten, V. A. (1983). *Physics of meteoric phenomena* (p. 356). Dordrecht, Holland: Kluwer.

Chau, J. L., Strelnikova, I., Schult, C., Oppenheim, M. M., Kelley, M. C., Stober, G., & Singer, W. (2014). Nonspecular meteor trails from non-field-aligned irregularities: Can they be explained by presence of charged meteor dust? *Geophysical Research Letters*, 41, 3336–3343. https://doi.org/10.1002/2014GL059922

Dyrud, L. P., Urbina, J., Fentzke, J. T., Hibbit, E., & Hinrichs, J. (2011). Global variation of meteor trail plasma turbulence. *Annales de Geophysique*, 29(12), 2277–2286. https://doi.org/10.5194/angeo-29-2277-2011

Ellyett, C. D., & Goldsbrough, P. F. (1976). Relationship of meteors to sporadic E: 1. A sorting of facts. *Journal of Geophysical Research*, 81(34), 6131–6134. https://doi.org/10.1029/JA081i034p06131

Enell, C.-F., Kozlovsky, A., Turunen, T., Ulich, T., Välitalo, S., Scotto, C., & Pezzopane, M. (2016). Comparison between manual scaling and Autoscala automatic scaling applied to Sodankylä Geophysical Observatory ionograms. *Geoscientific Instrumentation, Methods and Data Systems*, 5(1), 53–64. https://doi.org/10.5194/gi-5-53-2016

Fentzke, J. T., Janches, D., & Sparks, J. J. (2009). Latitudinal and seasonal variability of the micrometeor input function: A study using model predictions and observations from Arecibo and PFISR. *Journal of Atmospheric and Solar-Terrestrial Physics*, 71(6-7), 653–661. https://doi.org/10.1016/j.jastp.2008.07.015

Fentzke, J. T., Janches, D., Strelnikova, I., & Rapp, M. (2009). Meteoric smoke particle properties derived using dual-beam Arecibo UHF observations of D-region spectra during different seasons. *Journal of Atmospheric and Solar-Terrestrial Physics*, 71(17-18), 1982–1991. https://doi.org/10.1016/j.jastp.2009.09.002

Gritsevich, M., Lyytinen, E., Moilanen, J., Kohout, T., Dmitriev, V., Lupovka, V., et al. (2014). First meteorite recovery based on observations by the Finnish Fireball Network. In J.-L. Rault, & P. Roggemans (Eds.), *Proceedings of the International Meteor Conference, International Meteor Organization* (pp. 162–169). France: Giron.

Hocking, W. K., Fuller, B., & Vandepeer, B. (2001). Real-time determination of meteor-related parameters utilizing modern digital technology. *Journal of Atmospheric and Solar - Terrestrial Physics*, 63(2-3), 155–169. https://doi.org/10.1016/S1364-6826(00)00138-3

Jenniskens, P. (2006). *Meteor showers and their parent comets* (p. 790). Cambridge, UK: Cambridge University Press.

Kelley, M. C., Kruschwitz, C. A., Gardner, C. S., Drummond, J. D., & Kane, T. J. (2003). Mesospheric turbulence measurements from persistent Leonid meteor train observations. *Journal of Geophysical Research*, 108(D8), 8454. https://doi.org/10.1029/2002JD002392

Kim, J.-H., Kim, Y. H., Jee, G., & Lee, C. S. (2012). Mesospheric temperature estimation from meteor decay times of weak and strong meteor trails. *Journal of Atmospheric and Solar-Terrestrial Physics*, 89, 18–26. https://doi.org/10.1016/j.jastp.2012.07.003

Kozlovsky, A., Lukianova, R., Shalimov, S., & Lester, M. (2016). Mesospheric temperature estimation from meteor decay times during Geminids meteor shower. *Journal of Geophysical Research: Space Physics*, 121, 1669–1679. https://doi.org/10.1002/2015JA022222

Kozlovsky, A., Shalimov, S., & Lester, M. (2017). Mesospheric plasma irregularities caused by the missile destruction on 9 December 2009. *Journal of Geophysical Research: Space Physics*, 122, 6696–6707. https://doi.org/10.1002/2017JA024300

Kozlovsky, A., Shalimov, S., Lukianova, R., & Lester, M. (2014). Ionospheric effects of the missile destruction on 9 December 2009. *Journal of Geophysical Research: Space Physics*, 119, 3873–3882. https://doi.org/10.1002/2013JA019531

Kozlovsky, A., Turunen, T., & Ulich, T. (2013). Rapid-run ionosonde observations of traveling ionospheric disturbances in the auroral ionosphere. *Journal of Geophysical Research: Space Physics*, 118, 5265–5276. https://doi.org/10.1002/jgra.50474

Lee, C. S., Younger, J. P., Reid, I. M., Kim, Y. H., & Kim, J.-H. (2013). The effect of recombination and attachment on meteor radar diffusion coefficient profiles. *Journal of Geophysical Research: Atmospheres*, 118, 3037–3043. https://doi.org/10.1002/jgrd.50315

Lukianova, R., Kozlovsky, A., & Lester, M. (2017). Climatology and inter-annual variability of the polar mesospheric winds inferred from meteor radar observations over Sodankylä (67N, 26E) during solar cycle 24. *Journal of Atmospheric and Solar-Terrestrial Physics*, 171, 241–249. https://doi.org/10.1016/j.jastp.2017.06.005

Maruyama, T., Kato, H., & Nakamura, M. (2003). Ionospheric effects of the Leonid meteor shower in November 2001 as observed by rapid run ionosondes. *Journal of Geophysical Research*, 108(A8), 1324. https://doi.org/10.1029/2003JA009831

Maruyama, T., Kato, H., & Nakamura, M. (2008). Meteor-induced transient sporadic E as inferred from rapid-run ionosonde observations at midlatitudes. *Journal of Geophysical Research*, 113, A09308. https://doi.org/10.1029/2008JA013362

Oppenheim, M. M., Dyrud, L. P., & Ray, L. (2003). Plasma instabilities in meteor trails: Linear theory. *Journal of Geophysical Research*, 108(A2), 1063. https://doi.org/10.1029/2002JA009548

Schult, C., Stober, G., Keuer, D., & Singer, W. (2015). Radar observations of the Maribo fireball over Juliusruh: Revised trajectory and meteoroid mass estimation. *Monthly Notices of the Royal Astronomical Society*, 450(2), 1460–1464. https://doi.org/10.1093/mnras/stv614

Shalimov, S., & Kozlovsky, A. (2015). Diffuse spreading of inhomogeneities in the ionospheric dusty plasma. *Plasma Physics Reports*, 41(8), 645–650. https://doi.org/10.1134/S1063780X15080097

Stempels, E., & Kero, J. (2016). The Swedish Allsky Meteor Network: First results. In A. Roggemans, & P. Roggemans (Eds.), *Proceedings of the International Meteor Conference, International Meteor Organization* (pp. 288–290). Netherlands: Egmond.

Trakhtengerts, V. Y. (1994). Generation mechanism of polar mesosphere summer echoes. *Journal of Geophysical Research*, 99(D10), 21,083–21,088. https://doi.org/10.1029/93JD03280